Tectonophysics 815 (2021) 229007

Contents lists available at ScienceDirect

Tectonophysics

journal homepage: www.elsevier.com/locate/tecto

A fine crustal structure and geodynamics revealed by receiver functions along the Guangchang-Putian line in the Cathaysia Block, South China

Yongqian Zhang [a,b,*], Danian Shi [a,b], Qingtian Lü [a,b,*], Yao Xu [a,b], Zhiwu Xu [a,b], Xuejing Gong [a,b], Jiayong Yan [a,b], Tao Xu [c]

[a] Chinese Academy of Geological Sciences, Beijing 100037, China
[b] China Deep Exploration Center-SinoProbe Center, China Geological Survey & Chinese Academy of Geological Sciences, Beijing 100037, China
[c] Stake Key Laboratory of Lithospheric Evolution, Institute of Geology and Geophysics, Chinese Academy of Sciences, Beijing 100029, China

ARTICLE INFO

Keywords:
South China
Cathaysia Block
Zhenghe-Dapu fault
Receiver function
Crustal structure

ABSTRACT

The Cathaysia Block is located in South China, along the western margin of the Pacific plate, and well known for its widespread granitoids and rich poly-metallic mineralization. Despite the numerous studies conducted in this region, some key questions are still in debate, which revolve around the detailed crustal architecture, the boundary between the western and eastern part of Cathaysia Block, and the geodynamic evolution and metallogenic settings in the Cathaysia Block. In this study, we have conducted a dense broad-band seismic observation in the Cathaysia Block, and obtained the fine crustal structure of it by using P-wave receiver functions and analyzing other geophysical and geological studies comprehensively. Our study has following findings: (1) the crust of the Cathaysia Block is ~31.5 km thick, thinner than that of the global continent, and is interpreted to have been thinned since the Late Mesozoic; (2) the Vp/Vs ratio of the Cathaysia Block is lower than that of the global continent, which implies there is no extensive underplating beneath the Cathaysia Block, or that the magma may be confined at bottom of the crust and formed a velocity gradient belt around Moho; (3) Zhenghe-Dapu fault is marked as the structural boundary between the western and eastern Cathaysia Block; (4) the western and eastern Cathaysia Block have different intra-crustal structures, petrochronology features and mineralization settings; (5) the subduction of the paleo-Pacific plate and the following roll-back could be responsible for the geodynamic evolution of the crustal deformation, as well as the widespread magmatism and mineralization.

1. Introduction

Located along the western margin of the Pacific plate, the Cathaysia Block (CB) is makes up the South China Block by accretion with the Yangtze block along the Jiangshan-Shaoxing fault (JSF) (Fig. 1A). Tectonically, the CB can be divided into two units: the western Cathaysia block (WCB) and the eastern Cathaysia block (ECB), bounded by the Zhenghe-Dapu fault (ZDF, Chen and Jahn, 1998; Xu et al., 2007) or the North West Fujian Fault (NWFF, Lin et al., 2018). The CB is also well known for its widely distributed granitoids and poly-metallic mineralization formed in the Late Mesozoic (Cawood et al., 2013; Li et al., 2012; Shu et al., 2009; Sun et al., 2012; Wang et al., 2003, 2013; Zhang et al., 2013a). The Mesozoic granitoids and volcanic rocks in the CB are distributed spatially in belt, and tend to become younger southeastward. Since major geological events and deep processes could leave footprints of different scales in continental crust, making it the archive of geodynamic evolution (Hawkesworth et al., 2013; Blewett et al., 2010), the crustal architecture, the intra-crustal deformations and properties are responsible for the related geodynamical evolution and mineralization settings. Over the past decades, a good number of geophysical studies have been conducted in different parts of the CB, including the teleseismic tomography (e.g. Zhao et al., 2012), the receiver functions (e.g. He et al., 2013; Huang et al., 2015; Li et al., 2013, 2014b; Song et al., 2017; Wei et al., 2016; Zhang et al., 2021), the surface wave and ambient noise tomography (e.g. Li et al., 2018; Shen et al., 2016; Wang et al., 2017; Zhou et al., 2012), the shear wave splitting (e.g. Yang et al., 2019), the wide-angle reflection/ refraction (WARR) seismic soundings (e.g. Zhang et al., 2005, 2013b; Deng et al., 2011; Lin et al., 2020, 2021; Cai et al., 2016), the deep reflection seismics (DRS) (e.g. Dong et al., 2020; Lü et al., 2015), and the gravity modeling (e.g. Deng et al., 2014).

* Corresponding authors at: Chinese Academy of Geological Sciences, Beijing 100037, China.
E-mail addresses: zyongqian@cags.ac.cn, zyq_imr@163.com (Y. Zhang), lqt@cags.ac.cn (Q. Lü).

https://doi.org/10.1016/j.tecto.2021.229007
Received 27 April 2021; Received in revised form 5 July 2021; Accepted 27 July 2021
Available online 31 July 2021

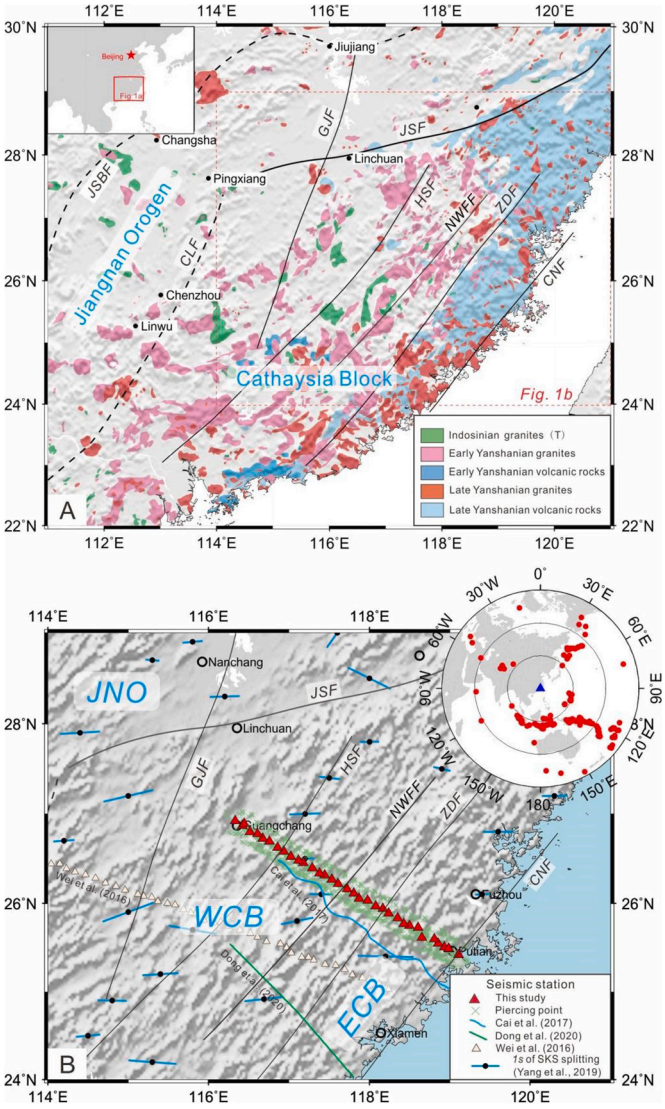

Fig. 1. (A) Location of our study area on an igneous rocks distribution map of the Cathaysia Block, South China. The data of the igneous rocks are from Zhou et al. (2006), the insert map denotes panel (A) in China mainland, and the dashed red rectangle in panel (A) denotes the locations of panel (B). (B) Locations of the seismic survey profiles used in this study. The insert map denotes the earthquake events used in this study with respect to the center of the GP-line (blue triangles). The light blue bars denote the shear wave splitting measurements (Yang et al., 2019). The red triangles and green crosses denote the locations of the dense broad-band seismic stations and the piercing points for Ps converted waves at 32-km depth. The light yellow triangles, the blue and the green lines denote the locations of the seismic survey profile of Wei et al. (2016), Cai et al. (2016) and Dong et al. (2020), respectively. The abbreviations for tectonics and faults are as follows: JNO: Jiangnan Orogen, WCB: Western Cathaysia Block, ECB: Eastern Cathaysia Block, JSBF: Jiujiang-Shitai Buried Fault, JSF: Jiangshan-Shaoxing Fault, CLF: Chenzhou-Linwu Fault, HSF: Heyuan-Shaowu Fault, NWFF: North West Fujian fault, ZDF: Zhenghe-Dapu fault, CNF: Changle-Nanao fault. (For interpretation of the references to colour in this figure legend, the reader is referred to the web version of this article.)

All these studies have suggested that the CB is characterized by a relatively thin crust and a flat Moho, which could be attributed to different geodynamic processes (e.g. Dong et al., 2020; Guo et al., 1983; Hsü et al., 1988, 1990; Jiang et al., 2015; Li et al., 2012, 2014a, 2017a; ; Li and Li, 2007; Mao et al., 2004, 2013; Shu et al., 2009, 2011, 2015; Sun et al., 2007, 2012; Wang et al., 2003; Zhou and Li, 2000, Zhou et al., 2006), like the Andean-type active continental margin (Guo et al., 1983), the Alpine-type collision belt (Hsü et al., 1988, 1990), and the paleo-Pacific plate subduction (e.g. Dong et al., 2020; Jiang et al., 2015; Li et al., 2012, 2014a, 2017a; Li and Li, 2007; Mao et al., 2004, 2013; Shu et al., 2009, 2011, 2015; Sun et al., 2007, 2012; Wang et al., 2003; Zhou and Li, 2000; Zhou et al., 2006).

Despite some controversy, the subduction the paleo-Pacific plate has generally been taken as a model to explain the magmatic activities and poly-metal mineralization in the CB (e.g. Li and Li, 2007; Sun et al., 2007; Mao et al., 2013; Jiang et al., 2015; Wang et al., 2016; Zhou et al., 2006). Nevertheless, much dispute still dwell on the detailed crustal deformation, the contact relationship between the ECB and WCB, the geodynamic evolution and the metallogenic settings for the W—Sn and Au—Cu mineralization in the CB (Ni et al., 2021). For a better understanding of the crustal structure and geodynamic evolution of the CB, we have conducted a 330-km-long broad-band seismic profile, which is almost perpendicular to the major tectonic trends in the CB (Fig. 1B). In this paper, we will first present the observations of the fine crustal structure obtained from the P-wave receiver function imaging along this profile, and then discuss their implications for the tectonic evolution and metallic mineralization background in the CB.

2. Geological and mineralization settings

The CB is tectonically characterized by numerous Mesozoic basins of relatively small size, variable accumulation environment and a complex basin-granite relationship (Ren and Chen, 1989). From west to east, four regional scale faults are distributed across the Mesozoic basin-granite region of the CB (Shu et al., 2009): (1) the Jiangshan-Shaoxing fault (JSF), the boundary fault between the CB and the neighbouring Jiangnan Orogen (JNO) (Zhang et al., 2013b; Cawood et al., 2013); (2) the Ganjiang fault (GJF), a regional fault with different geophysical properties at depth and considered to be the south extension of the Tanlu fault (Teng et al., 2000); (3) the Zhenghe-Dapu fault (ZDF), a possible boundary fault between the western Cathaysia block and eastern Cathaysia block (Chen and Jahn, 1998; Xu et al., 2007); (4) the Changle-Nanao fault (CNF), a sinistral ductile shear zone along the coast line of South China (Wang and Lu, 2000). Apart from these regional faults, there are also some local–scale faults, including the Fuan-Nanjing fault (FNF), the North West Fujian fault (NWFF, suggested to be the boundary fault between WCB and ECB by Lin et al., 2018), and the Heyuan-Shaowu fault (HSF), dominantly in trending of NE-SW.

The WCB is primarily characterized by the early Yanshannian (190–140 Ma) magmatism and the basement composed of arc–like metasedimentary rocks with felsic intrusions (Cawood et al., 2013; Lin et al., 2018; Wang et al., 2013; Yu et al., 2009), whereas the basement of ECB is mostly overlain by a NNE-trending volcanic belt composed of rhyolite, andesite and some high-K calc-alkaline basalt (Xu et al., 2007). The Late Yanshannian (140–90 Ma) magmatism is widespread in the ECB, which contributes to the generation of large-scale volcanic-intrusive rocks. Likewise, the intense magma activities in the CB has resulted in the formation of large amount of poly-metallic mineralization, including giant W—Sn deposits and abundant large Cu-Au-Mo, Ta—Nb, REE and U deposits (e.g. Deng and Wu, 2001; Mao et al., 2004; Hu et al., 2008; Ishihara, 1984; Li et al., 2014a). Spatially, W—Sn mineralization mainly occurred in the WCB, while the Au—Cu mineralization concentrated in the neighborhood of the ZDF (Ni et al., 2021; Xu and Xie, 2005; Zhou and Li, 2000).

3. Data and methods

In order to obtain the fine crustal structure of the CB, we have conducted a broad-band seismic profile between Guangchang in Jiangxi Province and Putian in Fujian Province in China (hereafter referred to as GP-line) (Fig. 1 and Table 1). From April 2017 to June 2019, we deployed 35 portable broad-band seismic stations to form a 350-km long profile, with an average station interval of 10 km. As for instruments, we

Table 1
The average crustal thickness (H) and Vp/Vs ratio (κ) beneath each station of the Guangchang-Putian line.

Tectonic unit	Station	Latitude (°N)	Longitude (°E)	Elevation (m)	H (km)	Vp/Vs	dH	dVp/Vs	No. of RFs
ECB	A006	25.42	119.11	14	30.0	1.780	1.6	0.028	61
	A007	25.49	118.99	93	30.0	1.760	1.7	0.027	49
	A907	25.49	118.98	149	29.5	1.790	1.7	0.052	26
	A008	25.51	118.93	114	30.0	1.810	1.6	0.024	113
	A009	25.55	118.85	192	31.5	1.720	1.7	0.025	108
	A010	25.59	118.81	523	32.0	1.750	2.2	0.056	90
	A011	25.61	118.65	889	31.5	1.820	1.8	0.029	94
	A012	25.73	118.61	578	32.5	1.730	2.5	0.026	47
	A013	25.74	118.50	216	33.0	1.705	1.7	0.026	93
	A014	25.77	118.43	683	32.0	1.765	1.7	0.028	72
	A015	25.83	118.35	658	31.5	1.755	1.8	0.046	93
	A016	25.88	118.24	749	31.5	1.720	1.6	0.018	37
	A017	25.94	118.17	530	30.5	1.795	1.9	0.036	119
WCB	A018	25.97	118.08	200	32.5	1.690	1.7	0.022	110
	A019	26.03	117.98	731	31.5	1.740	1.9	0.041	114
	A020	26.05	117.87	464	32.0	1.700	1.9	0.028	113
	A021	26.11	117.81	433	31.0	1.770	1.6	0.042	119
	A022	26.16	117.72	773	30.5	1.795	1.5	0.033	106
	A023	26.22	117.61	149	31.0	1.750	1.7	0.028	87
	A024	26.27	117.53	234	31.5	1.725	1.7	0.030	80
	A025	26.31	117.44	300	31.0	1.740	1.8	0.031	122
	A026	26.34	117.38	217	31.5	1.745	1.6	0.102	111
	A027	26.39	117.29	349	32.0	1.740	1.8	0.049	120
	A028	26.45	117.17	429	33.5	1.705	1.8	0.030	120
	A029	26.48	117.12	444	33.0	1.715	2.1	0.034	102
	A030	26.52	117.02	353	29.5	1.815	1.7	0.031	117
	A031	26.58	116.93	427	29.5	1.810	1.7	0.028	112
	A032	26.62	116.86	593	32.0	1.760	1.6	0.021	121
	A033	26.69	116.76	364	33.5	1.725	1.9	0.032	109
	A034	26.72	116.67	427	32.5	1.730	1.6	0.031	72
	A035	26.78	116.61	455	33.0	1.685	1.6	0.023	60
	A036	26.80	116.51	360	32.5	1.695	1.7	0.031	87
	A037	26.87	116.42	189	32.5	1.695	1.7	0.018	6
	A837	26.89	116.44	197	31.5	1.720	2.0	0.038	47
	A038	26.92	116.33	142	32.0	1.730	1.8	0.039	114

used the Guralp CMG-3ESPCD seismometers (with bandwidth of 0.02–60s) and the Guralp CMG-3TDE seismometers (with bandwidth of 0.02–120 s), with the original sample rate of record being 50 sample-per-second at each station. During the 26-month observation, we recorded 257 earthquakes with good signal-to-noise ratio, magnitude (*Ms)* greater than 5.0 and epicentral distance between 30°- 90°, which were later used to extract the P-wave radial receiver functions. Fig. 1B shows the locations of the 257 earthquake hypocenters and the piercing points of converted rays at the Moho assumed at the depth of 32 km.

P-wave radial receiver function (PRF), the radial waveforms created by deconvoluting the vertical component from the radial component, can isolate the receiver site effects from other information contained in the teleseismic P- waveforms (Langston, 1979). This technique has been proved efficient in estimating the crustal thickness and Vp/Vs ratios beneath the seismic stations (Zhu and Kanamor, 2000). In data processing, we firstly filtered the P-wave waveforms in the frequency band of 0.03–1.5 Hz. Having rotated the three-component seismic records from Z, N, E to Z, R, T direction, we calculated the PRFs with the time-domain iterative deconvolution method (Ammon, 1991). After that, we inspected the waveforms of the PRFs artificially to eliminate the records

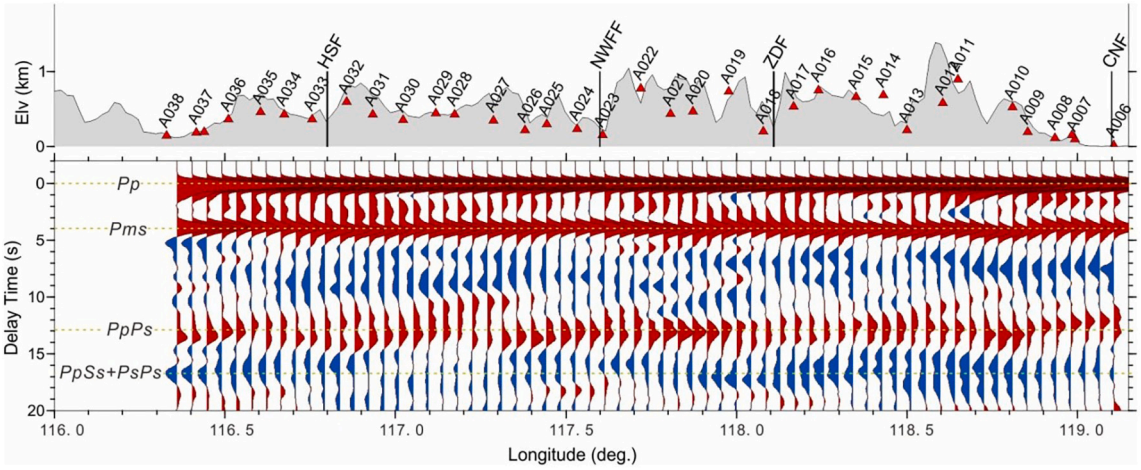

Fig. 2. Stacked receiver function profile in time-domain obtained by stacking of move-out corrected traces in 5-km bins, based on the locations of the piercing point at the depth of 32-km. The labeled dashed gray lines represent the seismic phases of Pp, Ps, PpPs, PpSs and PsPs. The upper panel denotes the topography and seismic stations along the GP-line, and the surface locations of the main faults shown in Fig. 1 are marked with vertical bars.

with low signal-to-noise ratio (SNR) for the Moho Ps conversions, and retained 3151 PRFs with good SNR for the next processes. By binning and stacking the move-out corrected PRF traces along the GP-line, in bins of 5-km-width based on the location of the piercing point at 32 km depth, we obtained the stacked PRFs, as shown in Fig. 2. In addition, the stacked PRFs from 4 different quadrants of NE, SE, SW and NW, which are shown in Fig. S1, enable us to get a general knowledge on the azimuth variations of the receiver functions.

In order to get the crustal thickness (H) and Vp/Vs ratio (κ) for individual stations, we have processed the available PRFs with the H-κ stacking estimates method (Zhu and Kanamor, 2000). From the original and stacked PRFs of stations A020, A010, A027 and A036, which are shown in Fig. 3 and Figs. S2–S4, in which we can see the different trends in the H-κ plane for the Ps phase and its multiples. By localizing the peak of the stacked function, we jointly determined the H and κ values (Zhang et al., 2014) by averaging velocities from the WARR seismic soundings (Cai et al., 2016; Lin et al., 2020, 2021). Synthetic tests show that the existence of azimuthal anisotropy and dipping Moho may influence the arrival times of the seismic phases, to a larger extent on crustal multiples than Ps (Li et al., 2017b). However, various regional seismic studies have shown that the Moho of South China is very flat (e.g. He et al., 2013; Huang et al., 2015; Li et al., 2014b; Song et al., 2017; Wei et al., 2016; Zhang et al., 2021), and the anisotropy in South China is almost in the same direction (Yang et al., 2019; Zhao et al., 2007). To further reduce the bias from anisotropy and dipping Moho, we tested different weight sets for Ps and its multiples (Fig. S5), and the results of which show little differences between each other. This has demonstrated the reliability of our results, suffered no first-order affection from either the dipping Moho or seismic anisotropy. Accordingly, the same procedures were applied to the rest stations, which procured the the 2-D variations of H and κ along the whole GP-line, as are shown in Table 1 and Fig. 4. In general, the statistical uncertainties of the H-κ stacking results along the GP-line are around 1.8 km for H and 0.026 for κ, respectively. The Vp/Vs ratio changes more drastically in the ECB and relatively smoothly in the WCB.

We have also deployed the Common Conversion Point (CCP)

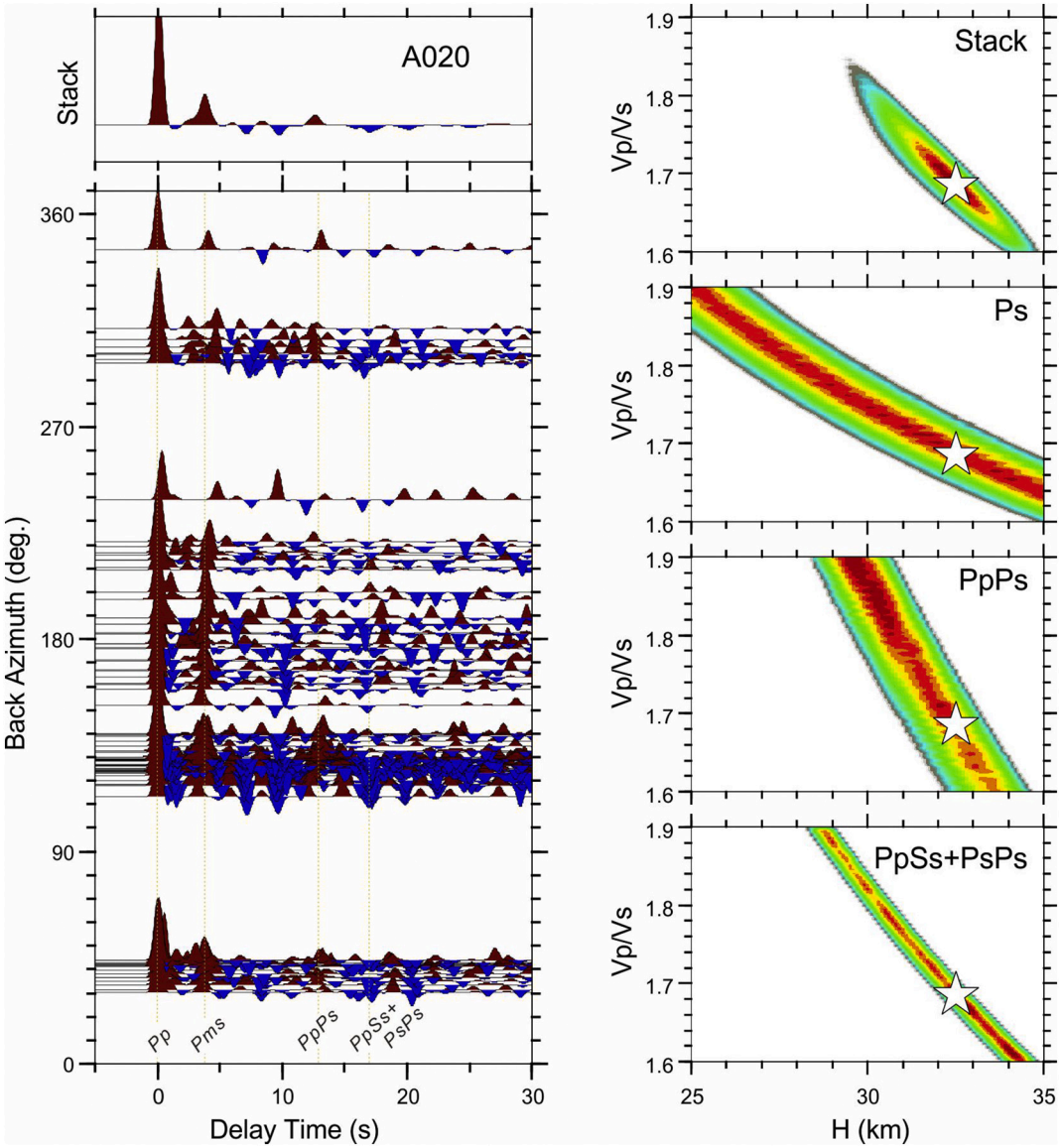

Fig. 3. H-κ stacking method estimating the crustal thickness (H) and average Vp/Vs ratio (κ) for station A020. Individual receiver functions ordered by back azimuth are shown on the left, in which the vertical lines indicates the Ps converted phase and its multiples. The upper left panel is the stacked receiver functions after move-out correction. The right panels show the amplitude plane of H vs. κ for Ps, PpPs, PpSs+PsPs phases and the stacked one, with the result values of H and κ marked by white stars.

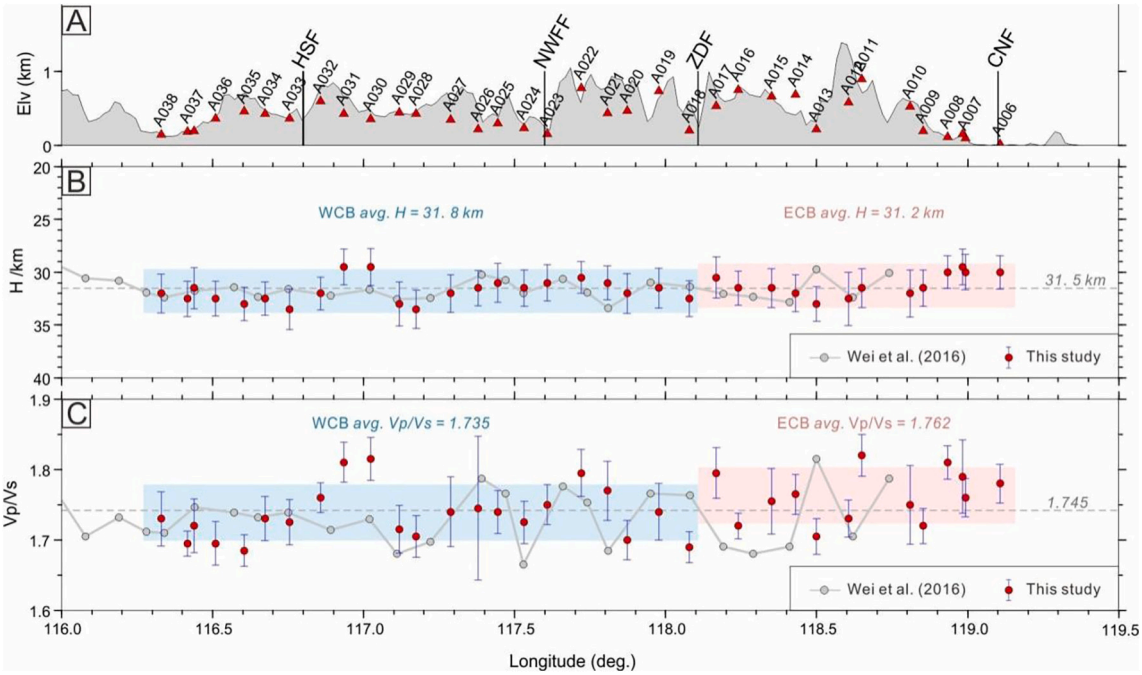

Fig. 4. The results of the H-κ stacking along the GP-line. (A) Topography and the main tectonics along the profile. (B) The crustal thickness (red circles) and estimated errors (gray bars) for all the 35 stations along the GP-line. (C) The Vp/Vs ratio (red circles) and estimated errors (gray bars) for all the 35 stations along the GP-line. Additionally, the light gray circles and lines in panels (B) and (C) are the results of Wei et al. (2016). The light blue and pink shadows mark the variance range of H and Vp/Vs ratio in the western and eastern Cathaysia Block. (For interpretation of the references to colour in this figure legend, the reader is referred to the web version of this article.)

stacking technique (Zhu, 2000) to image the crustal structure along the GP-line in depth-domain. The CCP stacking process contains two steps, the back projection and stacking. It firstly migrates the converted signal along the time series of PRFs to the spatial conversion locations based on a background velocity model; secondly, the crustal volume was divided into designated-size bins and all the amplitudes in the same bin were averaged to generate a spatial energy image, which can reveal the structural characteristics (Zhu, 2000; Zhang et al., 2018a, 2018b; Tian et al., 2020). In this study, we have deployed three kinds of information to constrain the background velocity model: (1) velocity model derived from WARR seismic soundings (Cai et al., 2016; Lin et al., 2021) was used to constrain the crustal velocity, (2) IASP91 velocity model (Kennett and Engdahl, 1991) was used to constrain the mantle velocity, and (3) the H and κ obtained in this study was used to constrain the crustal thickness and Vp/Vs ratio in the CCP imaging. Bins of 30-km wide (perpendicular to the line), 3-km long and 0.5 km thick were constructed along the GP-line in the CCP imaging of the crustal structure (Fig. 5c). This fine-constrained CCP image was proved robust and reliable by tests which use PRFs of earthquakes from different back-azimuths (Fig. S6). Moreover, the variation of the Moho discontinuity in the CCP image (Fig. 5c) is well consistent with the crustal thickness estimated by H-κ stacking, which further proves the reliability of our results.

4. Crustal structure of the Cathaysia Block

4.1. Crustal thickness and Vp/Vs ratio variation

The crustal thickness along the GP-line in this study could be determined by: the delay time between the P and Ps converted phases (t_{Ps}), the H value obtained from the H-κ stacking, and the depth of the maximum amplitude of the Ps phase. The t_{Ps} can reflect the Moho topography and be taken as the first-order constraints on the crustal thickness (Chen et al., 2015). In this study, the t_{Ps} is around 4.0 s in general (Fig. 2), which corresponds to a crust of about 32 km, and coincides well with that of the H-κ stacking (Fig. 4B) and CCP imaging (Fig. 5C). The good consistence of the results procured from the three methods have further improved the reliability and stability of the crustal thickness we got along the GP-line. Our results show that the average crustal thickness of the CB is ~31.5 km, which is comparable with that of the eastern North China Craton (NCC, ~32 km), but lower than those of the central NCC (~37 km), western NCC and Yangtze block (~42 km) (Wei et al., 2016), as well as that of the global continent (Christensen and Mooney, 1995). The discrepancy between the average crustal thickness of WCB (~ 31.3 km) and ECB (~31.8 km) is almost negligible, showing a flat Moho beneath the CB. Accordingly, we speculate that the flat and shallow Moho observed in the CB derives from the lithospheric extension since the Late Mesozoic, which will be discussed in detail in Section 5.

In addition, H-κ stacking also provides a quantitative estimate of the average crustal Vp/Vs ratio (κ) under each seismic station (Fig. 3), and we can thus get the Vp/Vs ratio variations along the GP-line by gathering all the individual station results (Fig. 4C). To conclude, the Vp/Vs ratio varies in a range of 1.68–1.82. The average value of Vp/Vs ratio along the GP-line is 1.745, which is lower than that of the global continent (~ 1.768, Christensen, 1996), indicating a more felsic composition in crust. Moreover, in the segment of ECB, the variation of Vp/Vs ratio shows a jitter characteristic and its average value is ~1.76, comparable to that of the global continent. However, in the segment of WCB, the average Vp/Vs ratio is 1.74, relatively lower than that of the eastern CB and the global average value.

4.2. Intra-crustal architectures

Features of the intra-crustal architectures, which appear as a series of positive amplitude phases with different dip directions and dip angles in the crust (Fig. 5D), can also be traced to the CCP image along the GP-line. For the convenience of discussion, we have labeled these intra-crustal seismic phases with L1 – L4 to the northwest of ZDF, and F1 – F4 to the southeast of ZDF. (1) The L1 – L4 phases vary smoothly in a depth range of ~15 to ~20 km in WCB, which, as we speculate, are the

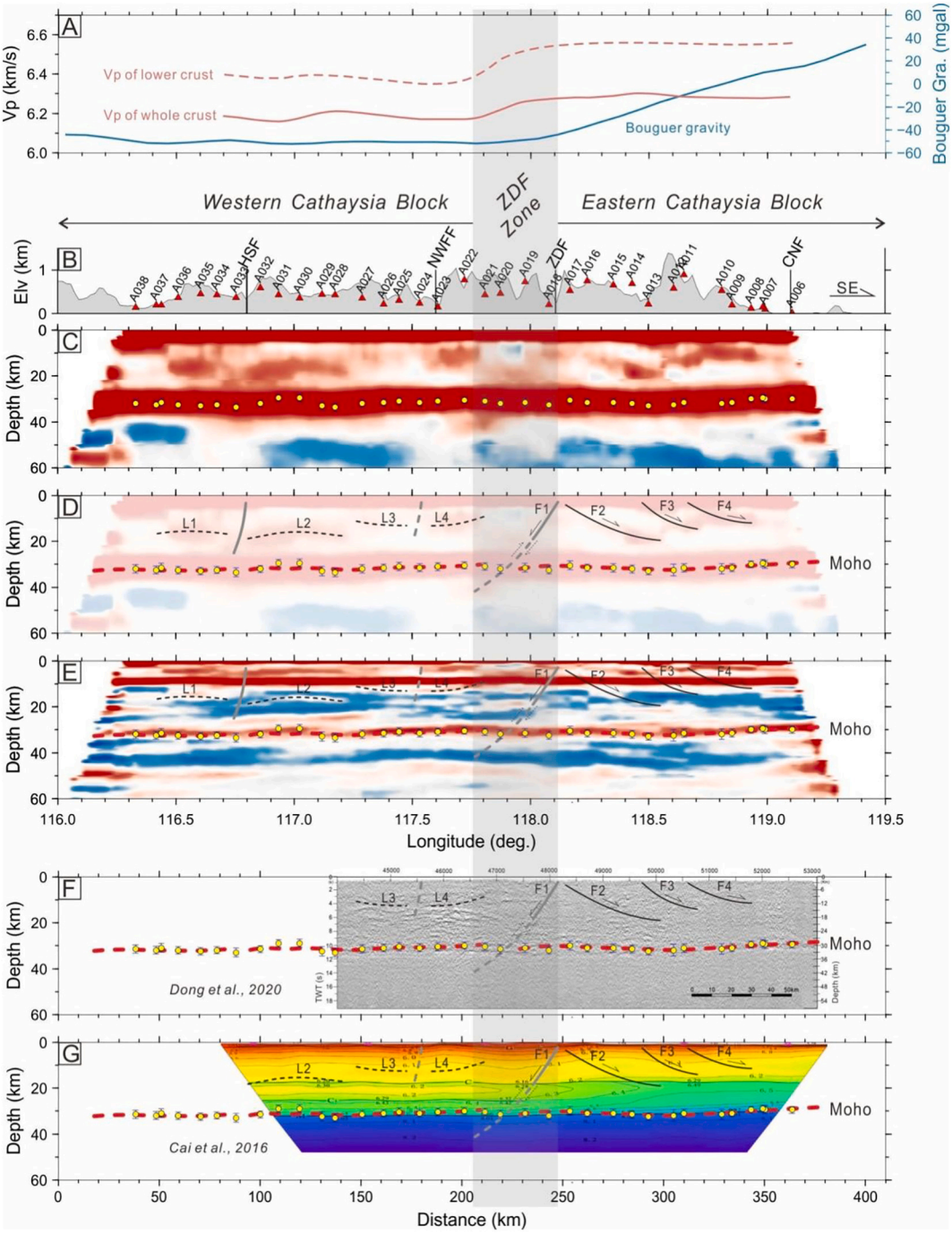

Fig. 5. Comprehensive geophysical observations along the GP-line. (A) Bouguer gravity anomaly (Zhang et al., 2021) and the average P-wave velocity for the whole crust and the lower crust of the nearby WARR profile (Cai et al., 2016; Lin et al., 2021). (B) Topography and locations of the broad-band seismic stations, also the main tectonics along the GP-line. (C) Depth-domain Common Conversion Points (CCP) imaging of the Ps phase of receiver functions along the GP-line, with H values (yellow dots) derived from H-κ stacking. (D) Interpretation on crustal architectures based on CCP imaging, in which the yellow dots indicate the H derived from H-κ stacking, the dashed red line indicate the Moho derived from CCP imaging, and L1 – L4, F1 – F4 mark the positive amplitude of CCP imaging. (E) CCP imaging of the PpPs phase of the seismic receiver functions. (F) Migrated seismic imaging of the nearby deep reflection seismic profile of Dong et al. (2020). (G) Velocity model of the nearby WARR seismic profile of Cai et al. (2016). The interpretations in (E)–(G) are the same as those in (D). (For interpretation of the references to colour in this figure legend, the reader is referred to the web version of this article.)

different segments of a high-velocity discontinuity. In order to confirm this speculation, we conducted a CCP imaging of the multiple-seismic phase PpPs along the GP-line, and identified well-developed multiples of the L1 –L4 phases in the PpPs- CCP images (Fig. 5E). (2) The F1 phase dips northwest with moderate-angle (~ 45°), and its location in the shallow part coincides with the ZDF. Thus, it is possible that the F1 phase is the trace of ZDF, and this result also coincides with the seismic migration imaging of a DRS profile (Dong et al., 2020) near the GP-line. (3) The F2, F3 and F4 phases dip southeast from the ground surface with low-angle (< 30°), but it is difficult to identify the multiples of the F2—F4 phases in the PpPs- CCP image, because the dipping interfaces always make the delay time of the multiple phases more divergent and hard to migrate their energy to the depth domain. Variations of such intra-crustal architecture are also noticeable in the time-domain stacked

PRFs (Fig. 2 and Fig. S1), which indicates different deformation styles in the crust of the WCB and ECB. Further interpretations on the formation of these intra-crustal seismic phases would be conducted in Section 5.

5. Discussions

5.1. Regional thinning of lithosphere and crust

It is feasible to evaluate the variation in deep crustal structure and geochemical composition with crustal thickness and Poisson's ratio, the seismic responses to tectonic process (Shu et al., 2009; Wong et al., 2011). As is mentioned in Section 4.1, the crust beneath the GP-line obtained in this study is ~31.5 km thick, conspicuously thinner than the average value of the global continent, which is considered to be 41 km (Christensen and Mooney, 1995; Mooney, 2007). This result also corresponds well with the results of other geophysical survey (Cai et al., 2016; Dong et al., 2020; Lin et al., 2021; Zhang et al., 2005, 2013b). WARR seismic sounding in the CB reveals Moho depth variations of 28.4–31.8 km from the coastal area to the inland of CB (Cai et al., 2016; Lin et al., 2021; Zhang et al., 2005, 2013b). DRS migration imaging suggests a crustal thickness of ~31–33 km beneath the CB, and shows that the Moho discontinuity performs as a narrow band of reflections beneath the WCB but as a gradient belt with a thickness of 2–3 km beneath the ECB (Dong et al., 2020). Regional teleseismic studies (He et al., 2013; Huang et al., 2015; Li et al., 2013, 2014b; Wei et al., 2016; Ye et al., 2013; Zhang et al., 2021) also suggest a thin crust beneath the CB. In addition to the thin crust, the lithosphere beneath the CB is also thinner (~ 60- 80 km from different studies), compared with the thick lithosphere (>80 km) in the Yangtze block (Deng et al., 2019, 2021; Wang et al., 2017; Zhang et al., 2018a, 2018b; Zheng et al., 2014; Zhou et al., 2012). However, according to the geochemical and petrological studies, South China used to have a thick crust (> 45 km) as well as a thick lithosphere (110–230 km) before the Late Mesozoic (Zhang et al., 2001; Zheng et al., 2015; Zhu et al., 2017). That is to say, the crust and lithosphere had been thinned by ~15 km and at least ~40 km, respectively, since the Late Mesozoic. Zhang et al. (2013b) computed the extensional factor and seismic reflection strength, and the results showed an eastward increase of extensional factors and strengthening of seismic reflections, indicating stronger extension in the east than the west of the CB. Lithospheric extension and/or other forms of mantle extrusion that have accompanied the subduction of the paleo-Pacific plate since the Late Mesozoic can account for the lithospheric and crustal thinning beneath the CB.

5.2. Vp/Vs ratio distribution and its implications for magma activities

As documented in Section 4.1, the average crustal Vp/Vs ratio along the GP-line is 1.745, while the values in WCB and ECB are 1.74 and 1.76, respectively. Vp/Vs ratio is directly related to Poisson's ratio (σ) through a formula of σ = 0.5–1(2*(κ*κ-1)), and Poisson's ratio is highly correlated with the composition of felsic materials of the crust. Hence, it is possible to evaluate the crustal composition by analyzing its Vp/Vs ratio distribution. Generally, the value of Vp/Vs ratio is negatively correlated with the content of felsic materials (Christensen, 1996; Ji et al., 2009). Ji et al. (2009) summarized the correlation of "crustal thickness (H) vs. Poisson's ratio (σ)", which could clue to the tectonic evolution of the continental crust. Considering the crust is composed of horizontal layers with felsic upper crust and mafic lower crust, the shortening and thickening in the felsic upper crust will lead to a decrease in Vp/Vs ratio with increasing crustal thickness. By contrast, the thickening in the mafic lower crust will lead to an increase in Vp/Vs ratio with increasing crustal thickness. In this study, the Vp/Vs ratios decrease linearly with increasing crustal thickness in the CB (Fig. 6), similar to that observed in the Baoding-Datong and Guanting-Zhang regions in North China (Ji et al., 2009), and Ji et al. (2009) argued that the "underplating of mafic magmas compensated the crustal thinning" could interpret such correlation.

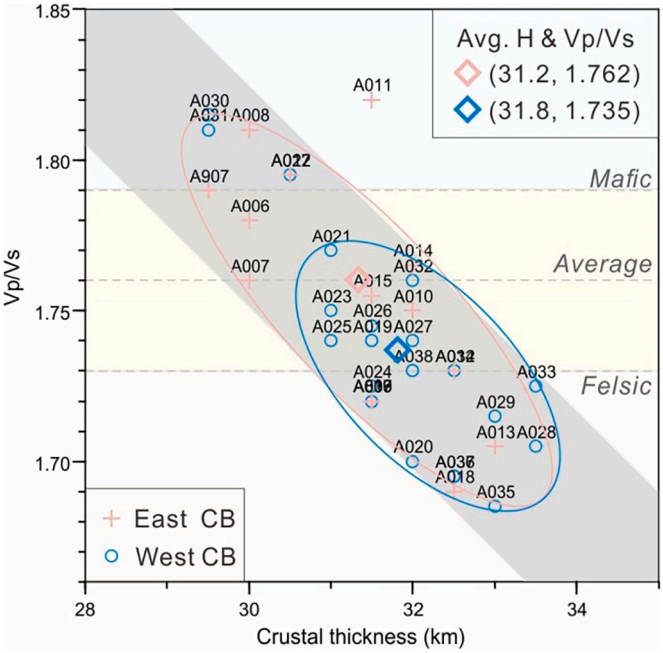

Fig. 6. H vs. κ for all the stations along the GP-line. The values in the western and eastern Cathaysia Blocks were respectively enclosed by individual best-fitting ellipses, and the diamonds at the center of each ellipse correspond to the average H and κ of the zone. The gray shadow denotes the liner decreasing of κ with increasing H. For reference, the three dashed lines indicate the κ values for mafic, felsic and average of global continent (Christensen, 1996).

In this study, the average value of the Vp/Vs ratios in the ECB is 1.76, which is slightly higher than that in the WCB, comparable with the average value of the global continent, but lower than the value of 1.79 required by mafic underplating in the lower crust (Christensen, 1996). In addition, the P-wave velocity model obtained from WARR (Cai et al., 2016; Lin et al., 2021) shows that the lower crust of ECB is featured with Vp 0f ~ 6.5 km/s, which is not compatible with the mafic or even ultramafic composition (with Vp > 7.0 km/s) required by lower crustal underplating (Thybo and Artemieva, 2013). Therefore, extensively strong underplating with large amount of mafic magma accumulated in the lower crust may not exist beneath the CB. Otherwise, if there had been large amount of underplated mafic magma in the lower crust of the CB, there must have been a strong extension or delamination at a later stage to offset the Vp and Vp/Vs ratio increase and crust thickening caused by the strong underplating (Deng et al., 2019; Zhang et al., 2021). Alternatively, the upwelling magma may only be confined to the bottom of the crust, which can result in a velocity gradient zone around Moho, and this style is also supported by the artificial seismic survey in the CB (Cai et al., 2016; Dong et al., 2020; Lin et al., 2021; Zhang et al., 2013b).

5.3. Intra-crustal deformation and the Zhenghe-Dapu fault

Sub-horizontal intra-crustal interfaces in WCB obtained in this study correspond well with the results of DSR migration imaging (Dong et al., 2020), in which the seismic reflectors are markedly stronger below the L2 – L4 interfaces. By incorporating with geological and geochronology studies, Dong et al. (2020) interpreted them as decollements, that reflect the inhomogeneous crustal shortening between Ordovician and Silurian. Such crustal shortening could also be responsible for the regional folds and thrusts formed during the period of ~460–420 Ma (Charvet et al., 2010; Shu et al., 2015; Li et al., 2017a). F2 —F4 obtained in this study are interpreted as extensional normal faults in the upper crust of ECB, which are consistent with the results obtained from WARR (Cai et al.,

2016; Lin et al., 2021) and DSR (Dong et al., 2020) studies. In the DSR migration profile (Fig. 5F), it looks more reflective beneath the F2 —F4 and more transparent above them, providing evidence for the existence of these faults in the viewpoint of wave impedance. In the velocity model derived from WARR experiments (Fig. 5G), it appears as higher velocity below the F2- F4 with lower velocity above them, confirming the nature of these faults as normal faults.

Whether the boundary between the WCB and the ECB is ZDF or NWFF has long been controversial. In this study, we tend to interpret F1 as ZDF, which could also be traced in the migration profile of DSR and velocity model of WARR. Although the nature of ZDF is still in debate (Xu et al., 2007; Shu et al., 2015; Li et al., 2017a), it is now widely accepted as a crustal-scale fault (Cai et al., 2016; Lin et al., 2021; Dong et al., 2020; Zhang et al., 2021). The segment of the CB on the eastern side of ZDF consists of widespread Yanshanian felsic igneous rocks, with few occurrences of basement rocks. By contrast, the segment of the CB on the western side of ZDF is featured by the presence of the Pre-Devonian strata, the Late Paleozoic to Triassic cover strata and the Yanshanian felsic igneous rocks (Shu et al., 2011). The crustal architecture and Vp/Vs ratio obtained in this study demonstrate contrasting properties on the two sides of ZDF, indicating a sub-horizontal intra-crustal deformation in WCB and extensional faults in ECB, respectively. To sum up, the crustal structure is consistent with the magmatic activities in the CB (Xu et al., 2007), and supports the viewpoint that ZDF is the boundary between the WCB and ECB.

5.4. *Insights for the geodynamics and minerallization in South China*

It is a consensus that the mineralization setting in the CB is featured by the dominant distribution of W—Sn in the western part and the concentricity of Au—Cu in the eastern part. Also, researchers generally accept that the metallogenesis is related to the deep crustal and upper mantle structure and geodynamic evolution in South China (Mao et al., 2004; Hu et al., 2008; Lü et al., 2021; Yang and Zhang, 2012; Wang et al., 2011). Nonetheless, the details of the ore-forming processes and geological settings are still in debate. The crustal architecture and Vp/Vs ratio properties obtained in this study can shed light on the possible mechanisms of the large-scale mineralization in the CB.

Geochronology studies have revealed that the magmatism had lasted for at least 100 Ma from the middle Jurassic to the early Cretaceous and migrated from inland to the southeast of CB (Xu et al., 2007; Zhou and Li, 2000). To be more specific, a two-stage process could be recognized according to the magmatic episodes (Fig. 7) (Ni et al., 2021). (1) From ~165 Ma to ~150 Ma: the W—Sn mineralization related magmatic activities in WCB mainly occurred in this period (Chen et al., 2013; Wang et al., 2020; and references therein). The tightly spatio-temporal relationship between A-type granitoids and the numerous giant W—Sn deposits indicates an extension mineralization setting. Besides, contemporaneous Au—Cu mineralization developed on the eastern side of ZDF, accompanied by a few mafic rocks dominantly clustering in Dehua. (2) From ~110 Ma to ~90 Ma: the widespread Au—Cu mineralization on the western side of ZDF mainly took place in this period (Ni et al., 2021; and references therein). The related magmatism has resulted in large-scale calc-alkaline felsic volcanic rocks, showing geochemical affinities with continental arc rocks in Dehua.

The seismic imaging of the crustal features obtained in this study are also consistent with the geochemical studies mentioned above. The flat and shallow Moho observed in this study and some other geophysical imaging (e.g. Zhang et al., 2013b; Zhang et al., 2018a, 2018b; Deng et al., 2019) indicate that the lithosphere of CB had been deconstructed by regional stretching and extending since the Late Jurassic, induced by the initiating of the paleo-Pacific subduction. Combining this study with previous geological and geochemical studies, we have created a cartoon model to illustrate the magma upwelling and mineralization mechanism in the CB (Fig. 8).

In the Early Yanshanian (Fig. 8A), the paleo-Pacific plate initiated to

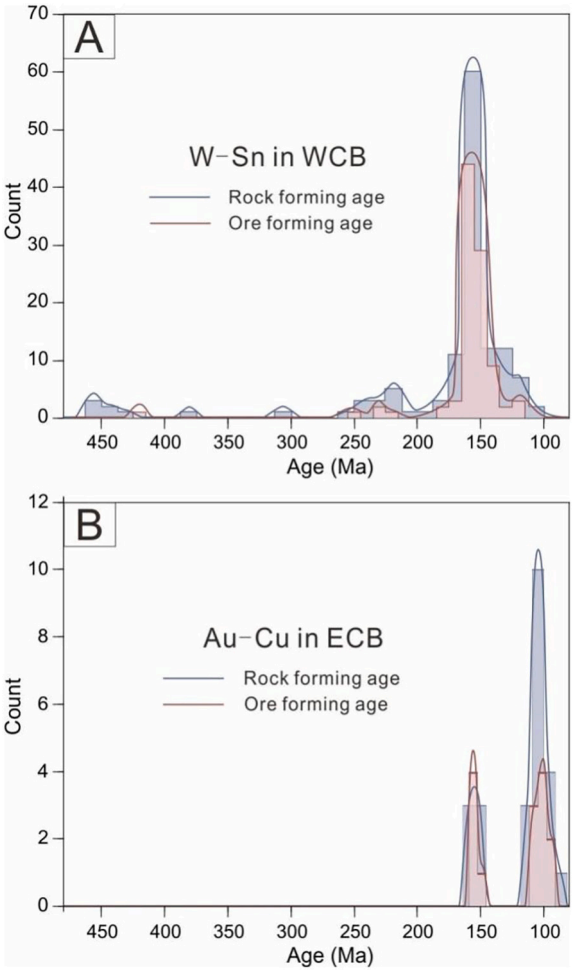

Fig. 7. Histogram of chronology data for the mineralization related rock-forming and ore-forming events (modified from Ni et al., 2021). (A) W—Sn related mineralization in the western Cathaysia Block, and (B) Au—Cu related mineralization in the eastern Cathaysia Block.

subduct underneath the CB. The dehydration of the subducted oceanic plate metasomatized mantle wedge, forming large-scaled arc-magma. Some of the arc-magma erupted as the volcanic rocks along the ZDF during ~165 Ma – ~150 Ma and formed the early stage Au—Cu deposits, while another portion underplated to form the juvenile lower crust. Simultaneously, far-field effects of the paleo-Pacific subduction caused the extension of the lithosphere and resulted in the thinning of the original crust (Groves et al., 2021). During this process, large amount of heat released from mantle led to the formation of A-type granites as well as W—Sn mineralization in the WCB. Further, the lithospheric and crustal thinning would decrease mafic/ultra-mafic components from the lower crust, and result in the low Vp/Vs ratio distribution observed in the CB. Higher Vp/Vs ratio in the ECB implies that the crust has undergone stronger magma activities than the WCB, in the form of magma upwelling. Although the Vp/Vs ratio and Vp in the ECB are higher than those in the WCB, they are lower than the value of mafic or even ultra-mafic crustal compositions (Christensen and Mooney, 1995; Christensen, 1996). It implies that the strength of magma activities is not strong enough to make large scaled underplating beneath the ECB. Instead, the deep magmas may be confined to the bottom of the lower crust and form a thin underplating layer near Moho. Such procedure would generate a velocity gradient belt around Moho, which had been observed by artificial seismic studies in ECB (Cai et al., 2016; Dong et al., 2020; Lin et al., 2021).

In the Late Yanshanian (Fig. 8B), as the subduction continued, the

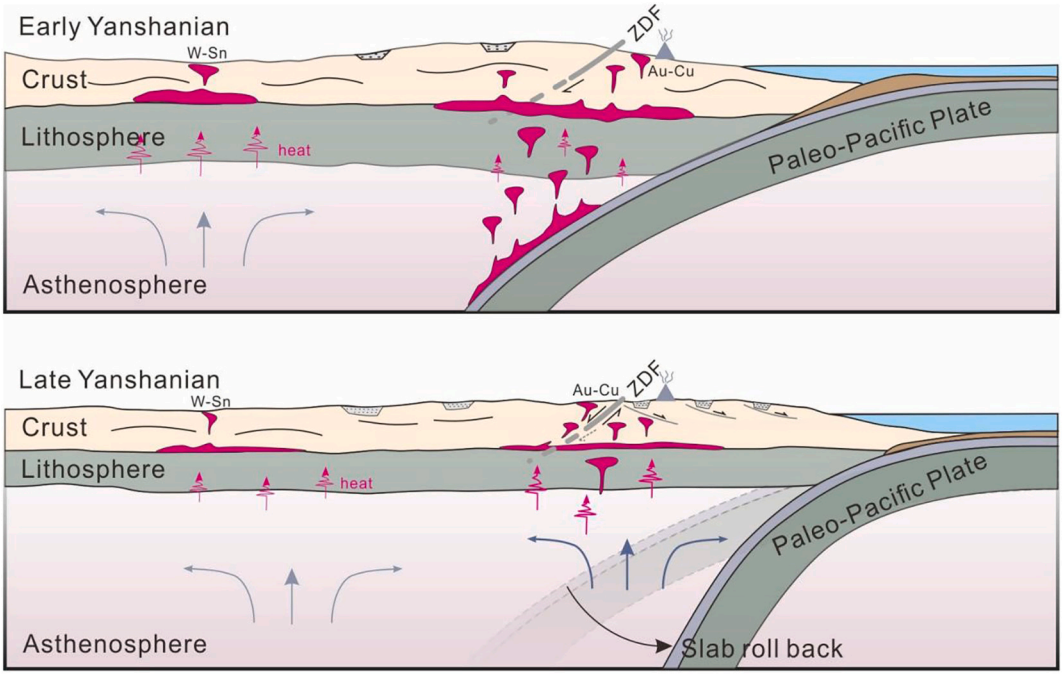

Fig. 8. Interpretative cartoon illustrating the two-stage subduction model of the paleo-Pacific plate. This model could be used to explicate the geodynamic evolution of the crustal structures observed in this study, as well as the widespread magmatism and poly-metallic mineralization in the Cathaysia Block. (A) In the Early Yanshanian, the initial low-angle subduction of paleo-Pacific plate caused the formation of the W—Sn related mineralization in the western Cathaysia Block and the Au—Cu related mineralization in the eastern Cathaysia Block; (B) In the Late Yanshanian, the colder and denser oceanic plate began to subduct at a steeper angle and roll back under gravity, causing strong extension and the related Au—Cu mineralization and bimodal volcanics.

colder and denser oceanic lithosphere sank more rapidly than the plate convergence, and the gravitationally unstable slab became steeper and rolled back. The roll-back of the paleo-Pacific slab caused retreat of the trench system as well as a strong extension environment. Such extension further thinned the lithosphere and crust beneath the CB, and transformed the circumstance from arc to back-arc settings (Ni et al., 2021). The tectonic activation in this period also caused ZDF to alter from a compressive reverse fault to an extensional normal fault. Besides, the metasomatized mantle wedge formed in the former stage remelted, the Au—Cu mineralization along ZDF (e.g. Zijinshan deposit) took place, and the coeval bimodal volcanic rocks as in Dehua area was finally formed.

6. Conclusions

Our study has provided new insights into the geodynamical and mineralization processes that the CB has undergone. By conducting a dense broad-band seismic observation along the GP-line, we have obtained a high-resolution seismic image of the crust beneath the CB, which reveals that the present crust of the CB is generally characterized by a shallow and flat Moho, low Vp and Vp/Vs ratio, compared with the average values of the global continent. Through comprehensive analyses of the geophysical and geochemical studies in this region, we conclude that the crustal architecture and properties in the CB have been strongly transformed since Yanshanian by the initiation of the paleo-Pacific subduction and the subsequent roll-back and retreat. The dehydration of the subducted paleo-Pacific plate metasomatized the mantle wedge, and formed large-scaled arc-magma and Au—Cu related mineralization in two periods. Moreover, the upwelling of the asthenospheric material and heat caused extensional environment for the overlying lithosphere and crust. Lithospheric extension resulted in the lithospheric and crustal thinning, as well as the decrease in the crustal Vp and Vp/Vs ratio decreasing. Finally, the different extensional strength in the two stages of the WCB and ECB led to the discrepancies in intra-crustal architectures, the formation of the granitoids and related mineralization in the WCB and ECB.

Declaration of Competing Interest

The authors declare that they have no known competing financial interests or personal relationships that could have appeared to influence the work reported in this paper.

Acknowledgements

We would like to express our gratitude to everyone that has made this work possible, especially the people who participated in the field work, including Jinhua Zhao, Yumin Gu, and other field personnel for their assistance. Our thanks also go to Prof. Laicheng Miao, Qiusheng Li, Dr. Hongshuang Zhang, Chunlin Li, Yunhao Wei and Wuyang Li for their thought-provoking discussions and suggestions. We also thank Ms. Ouyang Yu for her ungrudging help to polish the language. This study is financially supported by the National Key Research and Development Program of China (No. 2016YFC0600201) and the National Natural Science Foundation of China (Nos. 42074099, 41574082 and 41804093). Figures in this manuscript are originally plotted with GMT (Wessel and Smith, 1998).

Appendix A. Supplementary data

Supplementary data to this article can be found online at https://doi.org/10.1016/j.tecto.2021.229007.

References

Ammon, C.J., 1991. The isolation of receiver effects from teleseismic P waveforms. Bull. Seismol. Soc. Am. 81, 2504–2510.
Blewett, R.S., Henson, P.A., Roy, I.G., Champion, D.C., Cassidy, K.F., 2010. Scale-integrated architecture of a world-class gold mineral system: the Archaean eastern Yilgarn Craton, Western Australia. Precambrian Res. 183, 230–250.

Cai, H.T., Jin, X., Wang, S.X., Li, P., Chen, W., 2016. The crust structure and velocity structure characteristics beneath Ninghua-Datian-Hui'an. Chin. J. Geophys. 59 (1), 157–168. https://doi.org/10.6038/cjg20160113 (in Chinese with English abstract).
Cawood, P.A., Wang, Y.J., Xu, Y.J., 2013. Locating South China in Rodinia and Gondwana: a fragment of greater India lithosphere? Geology 41, 903–906.
Charvet, J., Shu, L.S., Faure, M., Choulet, F., Wang, B., Lu, H.F., Le, BretonN, 2010. Structural development of the lower Paleozoic belt of South China: genesis of an intracontinental orogeny. J. Asian Earth Sci. 39, 309–330. https://doi.org/10.1016/j.jseaes.2010.03.006.
Chen, J.F., Jahn, B.M., 1998. Crustal evolution of southeastern China: Nd and Sr isotopic evidence. Tectonophysics 284, 101–133.
Chen, J., Wang, R.C., Zhu, J.C., et al., 2013. Multipe-aged granitoids and related tungsten-tin mineralization in the Nanling Range, South China. Sci. Schina Earth Sci. 56, 2045–2055. https://doi.org/10.1007/s11430-013-4736-9.
Chen, Y., Xu, Y.G., Xu, T., Si, S.K., Liang, X.F., Tian, X.B., Deng, Y.F., Chen, L., Wang, P., Xu, Y.H., Lan, H.Q., Xiao, F.H., Li, W., Zhang, X., Yuan, X.H., Badal, J., Teng, J.W., 2015. Magmatic underplating and crustal growth in the Emeishan Large Igneous Province, SW China, revealed by a passive seismic experiment. Earth Planet. Sci. Lett. 432, 103–114. https://doi.org/10.1016/j.epsl.2015.09.048.
Christensen, N.I., 1996. Poisson's ratio and crustal seismology. J. Geophys. Res. 101 (B2), 3139–3156.
Christensen, N.I., Mooney, W.D., 1995. Seismic velocity structure and composition of the continental crust: a global view. J. Geophys. Res. 100 (B7), 9761–9788.
Deng, J.F., Wu, Z.X., 2001. Lithospheric thining event the Lower Yangtze craton and Cu-Fe metallogenic belt in the Middle and Lower Yangtze river reaches. Geol. Anhui 11 (2), 86–91 (in Chinese with English abstract).
Deng, Y.F., Li, S.L., Fan, W.M., et al., 2011. Crustal structure beneath South China revealed by deep seismic soundings and its dynamics implications. Chin. J. Geophys. 54 (10), 2560–2574 (in Chinese with English abstract).
Deng, Y.F., Zhang, Z.J., Badal, J., et al., 2014. 3-D density structure under South China constrained by seismic velocity and gravity data. Tectonophysics 627, 159–170.
Deng, Y.F., Li, J.T., Peng, T.P., et al., 2019. Lithospheric structure in the Cathaysia block (South China) and its implication for the Late Mesozoic magmatism. Phys. Earth Planet. Inter. 2019 (291), 24–34.
Deng, Y.F., Byrnes, J.S., Bezada, M., 2021. New insights into the heterogeneity of the lithosphere-asthenosphere system beneath South China from teleseismic body-wave attenuation. Geophys. Res. Lett. 48 https://doi.org/10.1029/2020GL091654 e2020GL091654.
Dong, S.W., Li, J.H., Cawood, P.A., Gao, R., Zhang, Y.Q., Xin, Y.J., 2020. Mantle influx compensates crustal thinning beneath the Cathaysia Block, South China: evidence from SINOPROBE reflection profiling. Earth Planet. Sci. Lett. 544, 116360. https://doi.org/10.1016/j.epsl.2020.116360.
Groves, D.I., Santosh, M., Zhang, L., Deng, J., Yang, L.Q., Wang, Q.F., 2021. Subduction: the recycling engine room for global metallogeny. Ore Geol. Rev. 104130 https://doi.org/10.1016/j.oregeorev.2021.104130.
Guo, L.Z., Shi, Y.S., Ma, R.S., 1983. On the formation and evolution of the Mesozoic-Cenozoic active continental margin and island arc tectonics of the western Pacific Ocean. Acta Geol. Sin. 1, 11–21 (in Chinese with English abstract).
Hawkesworth, C., Cawood, P., Dhuime, B., 2013. Continental growth and the crustal record. Tectonophysics 609, 651–660.
He, C.S., Dong, S.W., Santosh, M., et al., 2013. Seismic evidence for a geosuture between the Yangtze and Cathaysia Blocks, South China. Sci. Rep. 3 (1) https://doi.org/10.1038/srep02200.
Hsü, K.J., Sun, S., Li, J.L., Chen, H.H., Pen, H.P., Sengor, A.M.C., 1988. Mesozoic overthrust tectonics in south China. Geology 16, 418–421.
Hsü, K.J., Li, J.L., Chen, H.H., Wang, Q.C., Sun, S., Sengor, A.M.C., 1990. Tectonics of South China: key to understanding west Pacific geology. Tectonophysics 183, 9–39.
Hu, R.Z., Bi, X., Zhou, M.F., et al., 2008. Uranium metallogenesis in South China and its relationship to crustal extension during the cretaceous to Tertiary. Econ. Geol. 103, 583–598.
Huang, R., Xu, Y.X., Zhu, L.P., et al., 2015. Detailed Moho geometry beneath southeastern China and its implications on thinning of continental crust. J. Asian Earth Sci. 112, 42–48. https://doi.org/10.1016/j.jseaes.2015.09.002.
Ishihara, S., 1984. Granitoid series and Mo/W-Sn mineralization in east Asia. Geol. Surv. Jpn Rep. 263, 173–208.
Ji, S.C., Wang, Q., Salisbury, M.H., 2009. Composition and tectonic evolution of the Chinese continental crust constrained by Poisson's ratio. Tectonophysics 463, 15–30. https://doi.org/10.1016/j.tecto.2008.09.007.
Jiang, Y.H., Wang, G.C., Liu, Z., Ni, C.Y., Qing, L., Zhang, Q., 2015. Repeated slab advance-retreat of the Paleo-Pacific plate underneath SE China. Int. Geol. Rev. 57, 472–491.
Kennett, B.L.N., Engdahl, E.R., 1991. Traveltimes for global earthquake location and phase identification. Geophys. J. Int. 105, 429–465.
Langston, C.A., 1979. Structure under Mount Rainier, Washington, Inferred from teleseismic body waves. J. Geophys. Res. 84, 4749–4762.
Li, Z.X., Li, X.H., 2007. Formation of the 1300-km-wide intracontinental orogeny and postorogenic magmatic province in Mesozoic South China: a flat-slab subduction model. Geology 35, 179–182.
Li, S.Z., Santosh, M., Zhao, G.C., 2012. Intracontinental deformation in a frontier of super-convergence: a perspective on the tectonic milieu of the South China Block. J. Asian Earth Sci. 49, 313–329. https://doi.org/10.1016/j.jseaes.2011.07.026.
Li, Q.S., Gao, R., Wu, Francis T., et al., 2013. Seismic structure in the southeastern China using teleseismic receiver functions. Tectonophysics 606, 24–35.
Li, J.H., Zhang, Y.Q., Dong, S.W., et al., 2014a. Cretaceous tectonic evolution of South China: a preliminary synthesis. Earth Sci. Rev. 134, 98–136. https://doi.org/10.1016/j.earscirev.2014.03.008.
Li, Y.H., Gao, M.T., Wu, Q.J., 2014b. Crustal thickness map of the Chinese mainland from teleseismic receiver functions. Tectonophysics 611, 51–60. https://doi.org/10.1016/j.tecto.2013.11.019.
Li, J.H., Zhang, Y.Q., Zhao, G.C., Johnston, S.T., Dong, S.W., Koppers, A., Miggins, D.P., Sun, H.S., Wang, W.B., Xin, Y.J., 2017a. New insights into Phanerozoic tectonics of South China: early Paleozoic sinistral and Triassic dextral transpression in the east Wuyishan and Chencai domains, NE Cathaysia. Tectonics 36, 819–853. https://doi.org/10.1002/2016TC004461.
Li, J.T., Song, X.D., Zhu, L.P., Deng, Y.F., 2017b. Joint inversion of surface wave dispersions and receiver functions with P velocity constraints: application to Southeastern Tibet. J. Geophys. Res. Solid Earth 122, 7291–7310. https://doi.org/10.1002/2017JB014135.
Li, H.Y., Song, X.D., Lü, Q.T., Yang, X.Y., Deng, Y.F., Ouyang, L.B., Li, J.P., Li, X.F., Jiang, G.M., 2018. Seismic imaging of lithosphere structure and upper mantle deformation beneath east-central China and their tectonic implications. J. Geophys. Res. Solid Earth 123, 2856–2870. https://doi.org/10.1002/2017JB014992.
Lin, S.F., Xing, G.F., Davis, D.W., 2018. Appalachian-style mult-terrane Wilson cycle model for the assembly of South China. Geology 46 (4), 319–322. https://doi.org/10.1130/G39806.1.
Lin, J.Y., Tang, G.B., Xu, T., Cai, H.T., Lü, Q.T., Bai, Z.M., Deng, Y.F., Huang, M.F., Jin, X., 2020. Crustal P-wave velocity structure in upper crust and crystalline basement of the Qinhang and Wuyishan Metallogenic belts: constraint from the Wanzai-Hui'an deep seismic sounding profile. Chin. J. Geophys. 63 (12), 4396–4409. https://doi.org/10.6038/cjg2020O0158 (in Chinese with English Abstract).
Lin, J.Y., Xu, T., Cai, H.T., Lü, Q.T., Bai, Z.M., Deng, Y.F., Zhang, Y.Q., Huang, M.F., Badal, J., Jin, X., 2021. Crustal velocity structure of Cathaysia Block from an active-source seismic profile between Wanzai and Hui'an in SE China. Tectonophysics 811, 228874. https://doi.org/10.1016/j.tecto.2021.228874.
Lü, Q.T., Shi, D.N., Liu, Z.D., et al., 2015. Crustal structure and geodynamics of the Middle and Lower reaches of Yangtze metallogenic belt and neighboring areas: Insights from deep seismic reflection profiling. J. Asian Earth Sci. 114, 704–716.
Lü, Q.T., Meng, G.X., Zhang, K., Liu, Z.D., Yan, J.Y., Shi, D.N., Han, J.G., Gong, X.J., 2021. The lithospheric architecture of the Lower Yangtze Metallogenic belt, East China: insights into an extensive Fe-Cu mineral system. Ore Geol. Rev. 132, 103989. https://doi.org/10.1016/j.oregeorev.2021.103989.
Mao, J.W., Xie, G.Q., Li, X.F., et al., 2004. Mesozoic large scale mineralization and multiple lithospheric extension in South China. Earth Sci. Front. 11 (1), 45–55 (in Chinese with English Abstract).
Mao, J.R., Ye, H.M., Liu, K., et al., 2013. The Indosinian collision-extension event between the South China Block and the Palaeo-Pacific plate: evidence from Indosinian alkaline granitic rocks in Dashuang, eastern Zhejiang, South China. Lithos 172-173, 81–97.
Mooney, W.D., 2007. Crust and lithospheric structure – global crustal structure. Treatise Geophys. 1, 361–417.
Ni, P., Wang, G.G., Li, W.S., Chi, Z., Li, S.N., Gao, Y., 2021. A review of the Yanshanian ore-related felsic magmatism and tectonic settings in the Nanling W-Sn and Wuyi Au-Cu metallogenic belts, Cathaysia block, South China. Ore Geol. Rev. https://doi.org/10.1016/j.oregeorev.2021.104088.
Ren, J.S., Chen, T.Y., 1989. Tectonic evolution of the continental lithosphere in eastern China and adjacent areas. J. SE Asian Earth Sci. 3, 17–27.
Shen, W.S., Ritzwoller, M.H., Kang, D., Kim, Y., Lin, F.C., Ning, J.Y., Wang, W.T., Zheng, Y., Zhou, L.Q., 2016. A seismic reference model for the crust and uppermost mantle beneath China from surface wave dispersion. Geophys. J. Int. 206, 954–979. https://doi.org/10.1093/gji/ggw175.
Shu, L.S., Zhou, X.M., Deng, P., Wang, B., Jiang, S.Y., Yu, J.H., Zhao, X.X., 2009. Mesozoic tectonic evolution of the Southeast China Block: new insights from basin analysis. J. Asian Earth Sci. 34, 376–391. https://doi.org/10.1016/j.jseaes.2008.06.004.
Shu, L.S., Faure, M., Yu, J.H., Jahn, B.M., 2011. Geochronological and geochemical features of the Cathaysia block (South China): new evidence for the Neoproterozoic breakup of Rodinia. Precambrian Res. 187, 263–276. https://doi.org/10.1016/j.precamres.2011.03.003.
Shu, L.S., Wang, B., Cawood, P.A., Santosh, M., Xu, Z.Q., 2015. Early Paleozoic and Early Mesozoic intraplate tectonic and magmatic events in the Cathaysia Block, South China. Tectonics 34, 1600–1621. https://doi.org/10.1002/2015TC003835.
Song, P.H., Zhang, X.M., Teng, J.W., et al., 2017. Mohoimaging based on receiver function analysis with teleseismic wavefield reconstruction: application to South China. Tectonophysics 18, 118–131.
Sun, W.D., Ding, X., Hu, Y.H., Li, X.H., 2007. The golden transformation of the cretaceous plate subduction in the west Pacific. Earth Planet. Sci. Lett. 262, 533–542.
Sun, W.D., Yang, X.Y., Fan, W.M., 2012. Mesozoic large scale magmatism and mineralization in South China: preface. Lithos 150, 1–5.
Teng, J.W., Wang, G.J., Zhang, Z.J., Hu, J.F., 2000. Three-dimensional S-wave velocity structure of South China and the southward extension of Tan-Lu fault. Chin. Sci. Bull. 45 (23), 2492–2498.
Thybo, H., Artemieva, I.M., 2013. Moho and magmatic underplating in continental lithosphere. Tectonophysics 609, 605–619. https://doi.org/10.1016/j.tecto.2013.05.032.
Tian, X.B., Bai, Z.M., Klemperer, S.L., Liang, X.F., Liu, Z., Wang, X., Yang, X.S., Wei, Y.H., Zhu, G.H., 2020. Crustal-scale wedge tectonics at the narrow boundary between the Tibetan Plateau and Ordos block. Earth Planet. Sci. Lett. 554, 116700. https://doi.org/10.1016/j.epsl.2020.116700.
Wang, Z.H., Lu, H.F., 2000. Ductile deformation and 40Ar/39Ar dating of the Changle-Nanao ductile shear zone, southeastern China. J. Struct. Geol. 22, 561–570.

Wang, Y.J., Fan, W., Guo, F., et al., 2003. Geochemistry of Mesozoic mafic rocks adjacent to the Chenzhou-Linwu fault, South China: implications for the lithospheric boundary between the Yangtze and Cathaysia bocks. Int. Geol. Rev. 45, 263–286.
Wang, F.Y., Ling, M.X., Ding, X., et al., 2011. Mesozoic large magmatic events and mineralization in SE China: oblique subduction of the Pacific plate. Int. Geol. Rev. 53 (5–6), 704–726.
Wang, Y.J., Fan, W.M., Zhang, G.W., 2013. Phanerozoic tectonics of the South China block: key observations and controversies. Gondwana Res. 23, 1273–1305. https://doi.org/10.1016/j.gr.2012.02.019.
Wang, G.G., Ni, P., Zhao, C., Wang, X.L., Li, P., Chen, H., Zhu, A.D., Li, L., 2016. Spatiotemporal reconstruction of Late Mesozoic silicic large igneous province and related epithermal mineralization in South China: insights from the Zhilingtou volcanic-intrusive complex. J. Geophys. Res. Solid Earth 121, 7903–7928.
Wang, Q., Song, X., Ren, J., 2017. Ambient noise surface wave tomography of marginal seas in East Asia. Earth Planet. Phys. 1, 13–25.
Wang, D.H., Huang, F., Wang, Y., He, H.H., Li, X.M., Liu, X.X., Sheng, J.F., Liang, T., 2020. Regional metallogeny of Tungsten-tin-polymetallic deposits in Nanling region, South China. Ore Geol. Rev. 120, 103305. https://doi.org/10.1016/j.oregeorev.2019.103305.
Wei, Z.G., Chen, L., Li, Z.W., et al., 2016. Regional variation in Moho depth and Poisson's ratio beneath eastern China and its tectonic implications. J. Asian Earth Sci. 115, 308–320. https://doi.org/10.1016/j.jseaes.2015.10.010.
Wessel, P., Smith, W.H.F., 1998. New improved version of Generic Mapping Tools released. Eos Trans. AGU 79, 579. https://doi.org/10.1029/98EO00426.
Wong, J., Sun, M., Xing, G.F., et al., 2011. Ziron U-Pb and Hf isotopic study of Mesozoic felsic rocks from eastern Zhejiang, South China: geochemical contrast between the Yangtze and Cathaysia blocks. Gondwana Res. 19 (1), 244–259.
Xu, X.S., Xie, X., 2005. Late Mesozoic-Cenozoic basaltic rocks and crust-mantle interaction, SE China. Geol. J. China Univ. 11 (3), 318–334 (in Chinese with English abstract).
Xu, X.S., O'Reilly, S.Y., Griffin, W.L., et al., 2007. The crust of Cathaysia: age, assembly and reworking of two terranes. Precambrian Res. 158, 51–78. https://doi.org/10.1016/j.precamres.2007.04.010.
Yang, W., Zhang, H.F., 2012. Zircon geochronology and Hf isotopic composition of Mesozoic magmatic rocks from Chizhou, the lower Yangtze region: constraints on their relationship with Cu-Au mineralization. Lithos 150, 37–48. https://doi.org/10.1016/j.lithos.2012.06.026.
Yang, X.Y., Li, H.Y., Li, Y.H., Lü, Q.T., Zhang, G.B., Jiang, G.M., Li, X.F., 2019. Seismic anisotropy beneath eastern China from shear wave splitting. Geophys. J. Int. 218, 1642–1651.
Ye, Z., Li, Q.S., Gao, R., 2013. Seismic receiver functions revealing crust and upper mantle structure beneath the continental margin of southeastern China. Chin. J. Geophys. 56 (9), 2947–2958. https://doi.org/10.6038/cjg20130909.
Yu, J.H., Wang, L.J., Griffin, W.L., et al., 2009. A Paleoproterozoic orogeny recorded in a long-live cratonic remnant (Wuyishan terrane), eastern Cathaysia Block, China. Precambrian Res. 174, 347–363. https://doi.org/10.1016/j.precamres.2009.08.009.
Zhang, H.F., Sun, M., Lu, F.X., Zhou, X.H., Liu, Y.S., Zhang, G.H., 2001. Geochemical significance of a garnet lherzolite from the Dahongshan kimberlite, Yangtze craton, southern China. Geochem. J. 35 (5), 315–331. https://doi.org/10.2343/geochemj.35.315.
Zhang, Z.J., Badal, J., Li, Y., Chen, Y., Yang, L., Teng, J., 2005. Crust-upper mantle seismic velocity structure across southeastern Chian. Tectonophysics 395, 137–157.
Zhang, G.W., Guo, A.L., Wang, Y.J., et al., 2013a. Tectonics of South China continent and its implications. Sci. China Earth Sci. 56, 1804–1828. https://doi.org/10.1007/s11430-013-4679-1.
Zhang, Z.J., Xu, T., Zhao, B., Badal, J., 2013b. Systematic variations in seismic velocity and reflection in the crust of Cathaysia: new constraints on intraplate orogeny in the South China continent. Gondwana Res. 24, 902–917. https://doi.org/10.1016/j.gr.2012.05.018.
Zhang, Z.J., Wang, Y.H., Houseman, G.A., Xu, T., Wu, Z.B., Yuan, X.H., Chen, Y., Tian, X.B., Bai, Z.M., Teng, J.W., 2014. The Moho beneath western Tibet: shear zones and eclogitization in the lower crust. Earth Planet. Sci. Lett. 408, 370–377. https://doi.org/10.1016/j.epsl.2014.10.022.
Zhang, Y.Y., Chen, L., Ai, Y.S., Jiang, M.M., Xu, W.W., Shen, Z.Y., 2018a. Lithospheric structure of the South China block from S-receiver function. Chin. J. Geophys. 61 (1), 138–149 (in Chinese with English Abstract).
Zhang, H.S., Li, Q.S., Ye, Z., Gong, C., Wang, X.R., 2018b. New seismic evidence for continental collision during the assembly of the central Asian orogenic belt. J. Geophys. Res. Solid Earth 123, 6687–6702. https://doi.org/10.1029/2017JB0155061.
Zhang, Y.Q., Shi, D.N., Lü, Q.T., Xu, Y., Xu, Z.W., Yan, J.Y., Chen, C.X., Xu, T., et al., 2021. The crustal thickness and composition in the eastern South China Block constrained by receiver functions: Implications for the geological setting and metallogenesis. Ore Geol. Rev. 130, 103988. https://doi.org/10.1016/j.oregeorev.2021.103988.
Zhao, L., Allen, R.M., Zheng, T.Y., et al., 2012. High-resolution body wave tomography models of the upper mantle beneath eastern China and the adjacent areas. Geochem. Geophys. Geosyst. 13 (6) https://doi.org/10.1029/2012GC004119.
Zheng, T.Y., Zhao, L., He, Y.M., Zhu, R.X., 2014. Seismic imaging of crustal reworking and lithospheric modification in eastern China. Geophys. J. Int. 196, 657–670.
Zhao, L., Zheng, T.Y., Chen, L., Tang, Q.S., 2007. Shear wave splitting in eastern and central China: Implications for upper mantle deformation beneath continental margin. Phys. Earth Planet. Inter. 162, 73–84. https://doi.org/10.1016/j.pepi.2007.03.004.
Zheng, J.P., Lee, C.T.A., Lu, J.G., Zhao, J.H., Wu, Y.B., Xia, B., Li, X.Y., Zhang, J.F., Liu, Y.S., 2015. Refertilization-driven destabilization of subcontinental mantle and the importance of initial lithospheric thickness for the fate of continents. Earth Planet. Sci. Lett. 409, 225–231. https://doi.org/10.1016/j.epsl.2014.10.042.
Zhou, X.M., Li, W.X., 2000. Origin of Late Mesozoic igneous rocks in Southeastern China: implications for lithosphere subduction and underplating of mafic magmas. Tectonophysics 326, 269–287.
Zhou, X.M., Sun, T., Shen, W.Z., et al., 2006. Petrogenesis of Mesozoic granitoids and volcanic rocks in South China: a response to tectonic evolution. Episodes 29 (1), 26–33.
Zhou, L., Xie, J., Shen, W., Zheng, Y., Yang, Y., Shi, H., Ritzwoller, M.H., 2012. The structure of the crust and uppermost mantle beneath South China from ambient noise and earthquake tomography. Geophys. J. Int. 189 (3), 1565–1583.
Zhu, L.P., 2000. Crustal structure across the San Andreas Fault, southern California from teleseismic converted waves. Earth Planet. Sci. Lett. 179, 183–190.
Zhu, L.P., Kanamor, H., 2000. Moho depth variation in southern California from teleseismic receiver functions. J. Geophys. Res. 105, 2969–2980.
Zhu, K.Y., Li, Z.X., Xia, Q.K., Xu, X.S., Wilde, S.A., Chen, H.I., 2017. Revisiting Mesozoic felsic intrusions in eastern South China: spatial and temporal variations and tectonic significance. Lithos 294-295, 147–163. https://doi.org/10.1016/j.lithos.2017.10.008.